





Crystalline phases of laser-driven dipolar Bose-Einstein condensates

Chinmayee Mishra ¹, Stefan Ostermann ², Farokh Mivehvar ³, and B. Prasanna Venkatesh ¹

¹*Indian Institute of Technology Gandhinagar, Gandhinagar 382 355, India*

²*Department of Physics, Harvard University, Cambridge, Massachusetts 02138, USA*

³*Institut für Theoretische Physik, Universität Innsbruck, Technikerstraße 21a, 6020 Innsbruck, Austria*



(Received 14 July 2022; accepted 27 January 2023; published 16 February 2023)

Although crystallization is a ubiquitous phenomenon in nature, crystal formation and melting still remain fascinating processes with several open questions yet to be addressed. In this work we study the emergent crystallization of a laser-driven dipolar Bose-Einstein condensate due to the interplay between long-range magnetic and effectively infinite-range light-induced interactions. The competition between these two interactions results in a collective excitation spectrum with two-roton minima that introduce two different length scales at which crystalline order can emerge. In addition to the formation of regular crystals with simple periodic patterns due to the softening of one of the rotons, we find that both rotons can also soften simultaneously, resulting in the formation of exotic, complex periodic, or aperiodic density patterns. We also demonstrate dynamic state-preparation schemes for achieving all the crystalline ground states found for experimentally relevant and feasible parameter regimes.

DOI: [10.1103/PhysRevA.107.023312](https://doi.org/10.1103/PhysRevA.107.023312)

I. INTRODUCTION

Ultracold atomic gases with long-range interactions are a platform with unprecedented properties to realize exotic many-body phenomena in a well-controlled environment [1]. Long-range interactions in Bose-Einstein condensates (BECs) can either originate from the intrinsic magnetic dipole moment of atomic species [2–6] or be imposed by manipulating the BEC with external laser fields [7–16] or quantized dynamic cavity fields [17–20]. In addition to supersolid and crystalline (droplet array) phases precipitated by the long-range interactions, competition between diverse interactions in such systems can also lead to other interesting emergent physics. These include frustration in BECs confined to multimode cavities [21–23] and quasicrystalline order in dipolar BECs with spin-orbit interactions [24–26] or nondipolar BECs interacting with multiple cavities [27].

In this paper we focus on the interplay between long-range magnetic dipole and effectively infinite-range light-induced interactions in a cigar-shaped elongated BEC illuminated by two counterpropagating laser beams with orthogonal polarizations [see Fig. 1(a)]. In the absence of light this system is expected to exhibit a phase transition to supersolid [28–31] or droplet crystalline phases [32,33]. Alternately, it has been shown that for a nondipolar laser-driven BEC the translational invariance of the system can be broken, leading to the simultaneous formation of a crystalline atomic state and optical potential with an intrinsically chosen period comparable to that of the laser field's wavelength [10–12]. The formation of these phases is related to the instability of a magnetic [34,35] or a light-induced roton mode in the excitation spectrum [10–12], respectively, similar to the one originally predicted for superfluid ⁴He [36].

The fundamental question we pose here is the following: What are the phases that emerge from the competition

between these two distinct interactions? We show that this comprises an intriguing scenario leading to the formation of a rich variety of crystalline and supersolid phases. Specifically, from the collective excitation spectrum we find regimes with biroton softening arising from the competition between the two long-range interactions, indicating the existence of two possible crystallization length scales. We confirm this by calculating the ground-state phase diagram which hosts, besides the two individual ordered states corresponding to each long-range interaction, an intertwined emergent phase with periodic or aperiodic density patterns corresponding to the biroton softening. Ultimately, we outline state preparation schemes to achieve the different crystalline ground-state phases dynamically for experimentally feasible conditions.

The paper is organized as follows. In Sec. II we describe the system and set up the governing equations. In Sec. III we analyze the elementary excitations of a uniform condensate to demonstrate the emergence of the biroton spectrum. Section IV highlights the unique density modulations characterizing the crystalline ground states we obtain as a direct consequence of the various instabilities arising in the spectrum. In Sec. V we delineate the phase diagrams in terms of different observables demarcating the domains associated with various crystalline states found. The state preparation dynamics is detailed in Sec. VI. We summarize in Sec. VII. We provide some additional details that supplement the discussion in the paper in Appendixes A–E.

II. MODEL

We consider a dipolar BEC at zero temperature confined by a transverse harmonic trap with frequency ω_ρ in a cigar-shaped geometry in the z direction [see Fig. 1(a)]. The magnetic dipoles are oriented in the x direction. In addition,

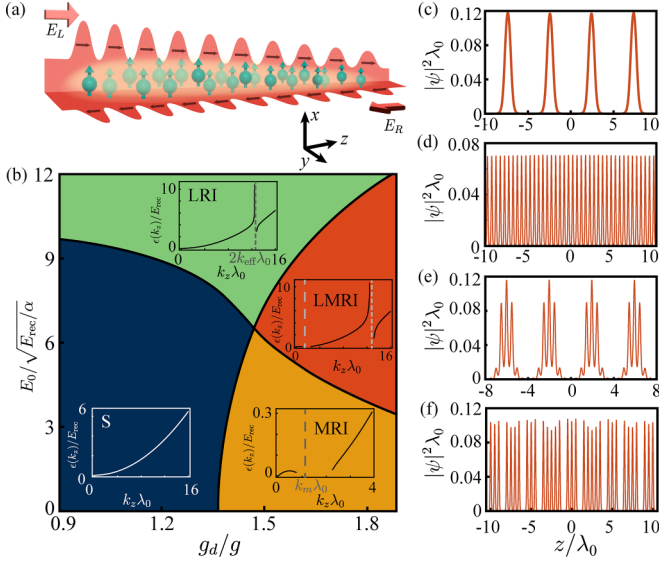


FIG. 1. (a) Schematic of a dipolar BEC in the presence of two counterpropagating laser beams of orthogonal polarization. (b) Stability diagram of a homogeneous BEC as a function of dipole-interaction strength g_d and light amplitude E_0 calculated from the excitation spectrum. The insets show examples of the typical spectrum that is stable (S) or consisting of either light roton instability (LRI) or magnetic roton instability (MRI), or biroton instability (LMRI). The gray dashed lines are a guide to the eye for the location of any roton instabilities. (c)–(f) Atomic density patterns in the crystalline ground-state phases. (c) Magnetic droplet crystal (MC) for $\{g_d/g, \sqrt{\alpha}E_0/\sqrt{E_{\text{rec}}}\} = \{1.52, 0\}$ and (d) light crystal (LC) for $\{g_d/g, \sqrt{\alpha}E_0/\sqrt{E_{\text{rec}}}\} = \{0.92, 12\}$. (e) and (f) Light-magnetic crystal (LMC) for $\{g_d/g, \sqrt{\alpha}E_0/\sqrt{E_{\text{rec}}}\} = \{1.42, 4.2\}$ and $\{1.7, 5\}$, respectively, for (e) droplets of supersolid and (f) an aperiodic crystal. Common parameters for (b)–(f) include $L = 50\lambda_0$, $\omega_\rho = 100E_{\text{rec}}/\hbar$, $\zeta = 0.1$, $a = 70a_0$ (a_0 is the Bohr radius), and $N = 10^5$ atoms.

the BEC is subject to two counterpropagating far-off resonant and orthogonally polarized, i.e., noninterfering, plane-wave laser beams. For atoms (with mass m) confined by an axial box potential $V_{\text{box}}(z)$ of extent L , the BEC order parameter is decomposed as $\Psi(\mathbf{r}, t) = \psi(z, t)e^{-(\eta x^2 + y^2)/2l^2}/\sqrt{\pi}l$, where the transverse width (anisotropy) l (η) remains a variational parameter following the reduced three-dimensional (3D) theory [37,38]. The dynamics of $\psi(z, t)$ is governed by the extended Gross-Pitaevskii equation (eGPE) including the Lee-Huang-Yang (LHY) correction term [32,33]

$$i\hbar\dot{\psi} = \left(\mathcal{E}_\rho - \frac{\hbar^2 \nabla_z^2}{2m} + V(z) + \Phi_\rho(z) + g_{\text{LHY}} N^{3/2} |\psi|^3 \right) \psi, \quad (1)$$

with $\int dz |\psi(z, t)|^2 = 1$. The interaction term is given by

$$\Phi_\rho = \frac{gN}{2\pi l^2} |\psi|^2 + \frac{gdN}{2\pi l^2} \int dk_z e^{ik_z z} V_d(k_z) n(k_z), \quad (2)$$

with the first term representing the short-range interaction of strength $g = 4\pi\hbar^2 a/m$ (a denoting the s -wave scattering length) and the second term the dipole-dipole interaction (DDI) with magnitude $gd = \mu_0 d^2/3$ for atoms with a dipole

moment d . Furthermore, $n(k_z)$ is the Fourier transform of the density and $V_d(k_z)$ is the dipole interaction in momentum space given by $V_d(k_z) = 3(1 - q^2 e^{q^2} \Gamma[0, q^2]) / (1 + \eta) - 1$, with $q = k_z^2 l^2 \sqrt{\eta}/2$ and $\Gamma[a, b]$ denoting the incomplete Gamma function. The transverse energy $\mathcal{E}_\rho = (\hbar^2/4ml^2 + ml^2\omega_\rho^2/4)(\eta + 1/\eta)$. The magnitude of the LHY correction term proportional to $|\psi|^3$ is given by $g_{\text{LHY}} = (64ga^{3/2}/15\pi^2 l^3)(1 + 3g_d^2/2g^2)$.

The potential $V(z)$ in Eq. (1) consists of $V_{\text{box}}(z) = 0$ if $|z| \leq L/2$ and ∞ otherwise and $V_{\text{opt}}(z)$ induced by the incoming light beams, i.e., $V(z) = V_{\text{box}}(z) + V_{\text{opt}}(z)$. The optical potential depends only on the sum of the individual intensity distributions of the left $E_L(z)$ and right $E_R(z)$ propagating laser fields as $V_{\text{opt}}(z) = -\alpha[|E_L(z)|^2 + |E_R(z)|^2]$, with α denoting the real part of the polarizability of the atoms. The laser fields individually satisfy the Helmholtz equation with the atomic density acting as a refractive medium,

$$\frac{\partial^2}{\partial z^2} E_{L,R}(z) + \frac{(2\pi)^2}{\lambda_0^2} [1 + \zeta \lambda_0 |\psi(z, t)|^2] E_{L,R}(z) = 0, \quad (3)$$

subject to appropriate boundary conditions (see Appendix A). Here $\lambda_0 = 2\pi/k_0$ denotes the wavelength of the incoming plane-wave laser field. The dimensionless quantity $\zeta = \alpha N/2\pi\epsilon_0 l^2 \lambda_0$ characterizes the coupling between the atomic density and the light. Note that for running-wave laser fields in the absence of the atomic backaction, $V_{\text{opt}}(z)$ amounts simply to a position-independent constant energy shift.

The coupled equations (1) and (3) have to be solved in conjunction with the minimization of the following energy functional with respect to the parameters l and η that determine the full 3D order parameter $\Psi(\mathbf{r}, t) = \psi(z, t)e^{-(\eta x^2 + y^2)/2l^2}/\sqrt{\pi}l$:

$$\mathcal{E}(\psi; l, \eta) = \mathcal{E}_\rho + \int dz \psi^*(z, t) \left(-\frac{\hbar^2}{2m} \nabla^2 + V(z) + \frac{\Phi_\rho}{2} + \frac{2g_{\text{LHY}} N^{3/2}}{5} |\psi|^3 \right) \psi(z, t). \quad (4)$$

The method used to solve the Helmholtz equations [10] is covered in Appendix A.

III. COLLECTIVE EXCITATIONS AND INSTABILITIES OF A HOMOGENEOUS CONDENSATE.

To understand the nature of the ground states of the coupled equations (1) and (3) in the absence of V_{box} , we analyze the collective excitation spectrum of the system by linearizing the equations of motion about a homogeneous atomic wave function $\psi_0(z) = 1/\sqrt{L}$ and plane-wave fields $E_{L,R}^0(z) = E_0 e^{\pm ik_{\text{eff}} z}$, with E_0 denoting the amplitude of the driving laser fields far away from the BEC. The effective propagation number $k_{\text{eff}} = 2\pi\sqrt{1 + \zeta\lambda_0|\psi(z)|^2}/\lambda_0$ in a homogeneous atomic cloud. We can write

$$\psi(z) = [\psi_0(z) + ue^{-i(k_{\text{eff}}z - \omega t)} + v^* e^{i(k_{\text{eff}}z - \omega t)}] e^{-i\mu t/\hbar},$$

$$E_{L,R}(z) = E_{L,R}^0(z) + \delta E.$$

Using the above *Ansätze* in Eqs. (1) and (3) and keeping terms up to linear order in the fluctuations δE , u , and v^* , the calculations are easily performed in Fourier space. The

expression for δE after reverting to position space is given by

$$\delta E = -\frac{(2\pi)^2 \zeta E_0}{\lambda_0 \sqrt{L}} \left(\frac{(u+v)e^{-i(k+k_{\text{eff}})+i\omega t}}{k_{\text{eff}}^2 - (k+k_{\text{eff}})^2} + \frac{(u^*+v^*)e^{i(k-k_{\text{eff}})-i\omega t}}{k_{\text{eff}}^2 - (k-k_{\text{eff}})^2} \right).$$

Using the above expression, the eGPE is linearized in a standard way. The resulting dispersion relation reads

$$\epsilon(k_z) = \left[\frac{\hbar^2 k_z^2}{2m} \left(\frac{\hbar^2 k_z^2}{2m} + \frac{gN}{\pi l^2 L} + \frac{g_d N}{\pi l^2 L} V_d(k_z) + \frac{3g_{\text{LHY}} N^{3/2}}{L^{3/2}} - \frac{32\pi^2 \zeta \alpha |E_0|^2}{L \lambda_0 (k_z^2 - 4k_{\text{eff}}^2)} \right) \right]^{1/2}. \quad (5)$$

Clearly, the spectrum has features from both the magnetic DDI and light-induced interactions (LIIs). Note that the terms corresponding to the interactions and the quantum fluctuation have a dependence on the variational parameters l and η , which are obtained from the minimization of a reduced form of the energy functional in Eq. (4),

$$\mathcal{E}_{\text{hom}} = \mathcal{E}_\rho + \frac{gN}{4\pi l^2 L} + \frac{g_d N}{4\pi l^2 L} \left(\frac{3}{1+\eta} - 1 \right) + \frac{2}{5} \frac{g_{\text{LHY}} N^{3/2}}{L^{3/2}} - 2\alpha E_0^2. \quad (6)$$

By looking at Eq. (5) it is clear that there exists a singularity at $k_z = 2k_{\text{eff}}$ which sets the light crystal (LC) periodicity [10]. In principle, this divergence is compensated by the infinitely large L where the reflection of incident light at the edge of the condensate boundary can be neglected, which is a purely finite-size effect incorporated in our model. The singularity is easily avoided by considering finite L which enforces quantization of the momentum values, i.e., k_z can only take discrete values in the multiple of $2\pi/L$. The divergence in the truly infinite L limit is a limitation of the model which can be overcome when the retardation effects of the light fields are taken into account.

In Fig. 1(b) we show the three distinct types of instabilities [$\epsilon^2(k_z) < 0$] which can occur in this system, according to Eq. (5), as a function of the strength of magnetic dipolar interaction g_d/g and the amplitude of the light fields E_0 .¹ Insets in Fig. 1(b) show the representative spectrum for each parameter region. We see that for a fixed small value of $\sqrt{\alpha} E_0 / \sqrt{E_{\text{rec}}} \lesssim 6$ the system develops a magnetic roton as g_d/g is increased. This roton eventually softens at the wave number k_m , signaling a transition from the stable (S) regime to the magnetic roton instability (MRI) regime [34]. Similarly, increasing E_0 at a fixed and sufficiently small $g_d/g \lesssim 1.3$ leads to a roton induced by the light fields. This roton softens at $2k_{\text{eff}}$ to enter the light roton instability (LRI) regime [10].

¹Note that in Figs. 1 and 2 g_d/g is varied by modifying the dipole moment as $7 < d/\mu_B < 10$ with a constant. Though not realistic from an experimental point of view, this helps in a direct comparison of the interplay purely between the two long-range interactions. Nonetheless, it is conceivable that every point on the phase diagram can also be attained by varying a for fixed values of d .

In addition to these expected instabilities where one of the two long-range interactions is dominant, we also find a third type of instability when both g_d/g and E_0 are comparatively strong to enter a biroton instability (LMRI) region. Here the magnetic and the light-induced rotons are simultaneously unstable.² As we discuss later, contributions from both wave numbers k_m as well as $2k_{\text{eff}}$ ($> k_m$) give rise to a new phase with periodic or aperiodic density patterns. Moreover, the nonlinearity of the phase boundaries in Fig. 1(b) clearly shows the interplay between the rotons. The S-LRI and MRI-LMRI transition boundaries are significantly altered when g_d/g is increased as the nonlinear dependence of DDI on k_z helps soften the higher momentum modes and lower the critical E_0 needed to instigate the transition. Alternately, an increase in E_0 pushes the S-MRI and LRI-LMRI transition boundaries to higher g_d/g values as the light fields counteract the unstable magnetic roton and cure it. This can be well understood by the low-momentum behavior of the spectrum ($k_z \ll 2k_{\text{eff}}$) where the last term in Eq. (5) becomes dominantly positive requiring a higher magnitude of g_d/g for magnetic roton softening. An important distinction between the two rotons is while LRI remains sharply peaked at $2k_{\text{eff}}$, the MRI can span a broad range of momenta. This greatly influences the density distribution of the corresponding ground states.

IV. PERIODIC AND APERIODIC CRYSTALLIZATION

In order to obtain the density-wave ground states precipitated from the various roton instabilities, we look for the stationary states of the system in the potential V_{box} of finite extent L .³ We employ imaginary-time evolution and conjugate gradient methods [40,41] along with a fourth-order Runge-Kutta method to simultaneously solve the eGPE (1) and the Helmholtz equation (3). Deep in the MRI and the LRI regimes a straightforward mapping exists to the stationary states of the magnetic crystal (MC) [see Fig. 1(c)] [34] and light crystal [see Fig. 1(d)] [10] phases, respectively. The periodicity of these density patterns for the MC (LC) is set by the softened momenta associated with the magnetic (light) roton.

Apart from these two known phases, the biroton instability engenders peculiar light-magnetic crystal (LMC) states, where the two long-range interactions compete with one another. This can result in density waves with either periodic or aperiodic order [see Figs. 1(e) and 1(f)] [42]. Figure 1(e) shows an example of the former. The density exhibits a periodic envelope of droplets (induced by the DDI) where each of them supports intradroplet crystals (set by the LII) of smaller periodicity, thus forming a unique ‘‘droplets of supersolid’’

²This biroton instability owes its existence to the distinct functional form of the two interactions considered here. It is not an immediate consequence of having two long-range interactions (see Ref. [39] for a counterexample).

³Note that within our present model, which neglects propagation effects in the Helmholtz equation, the usual thermodynamic limit $N, L \rightarrow \infty$ and finite N/L lead to diverging energy [10], while the modified thermodynamic limit $L \rightarrow \infty$ with finite N [10] nullifies the effect of dipole and contact interactions but keeps the light-induced interactions finite.

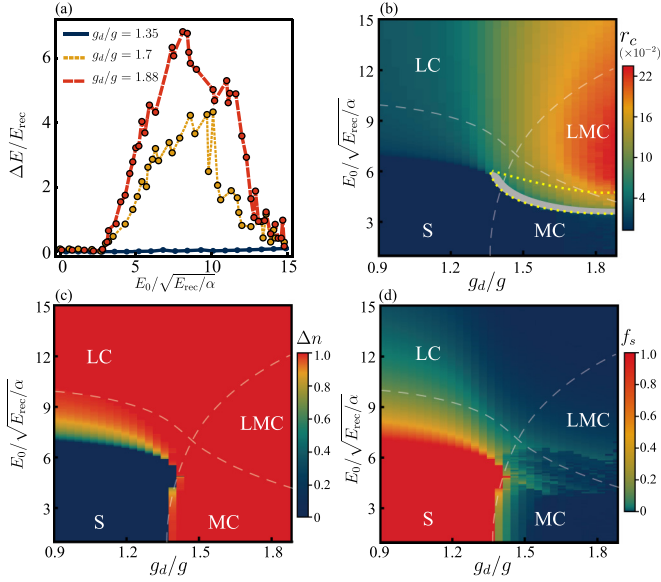


FIG. 2. (a) Maximum energy difference between converged states of the eGPE for six different initial guesses for three g_d/g values. (b)–(d) Mean-field phase diagram as a function of $\{g_d/g, \sqrt{\alpha}E_0/\sqrt{E_{\text{rec}}}\}$ characterized by (b) reflection coefficient r_c , (c) density contrast Δn , and (d) superfluid fraction f_s . White dashed lines are the stability diagram boundaries from the excitation spectrum. The yellow dotted curve demarcates the droplets of supersolid phase and the gray strip highlights the domain where density patterns are always periodic. All other parameters are the same as in Fig. 1(b).

state. Note that the parameters $g_d/g = 1.42$ and $\sqrt{\alpha}E_0 = 4.2\sqrt{E_{\text{rec}}}$ used for Fig. 1(e) indicate that the LII effects are prominent even below the LMRI threshold in Fig. 1(b) due to finite-size effects as discussed further below. This is in contrast to the aperiodic ordered pattern in Fig. 1(f) that is observed for higher E_0 values away from the MRI-LMRI boundary. The lack of discrete translational symmetry in such structures can be attributed to contributions from a broad range of momenta associated with the softened magnetic roton. Furthermore, note that the emergence of atomic density patterns shown in Figs. 1(d)–1(f) is accompanied by the development of a standing-wave light field [10] (see Appendix A).

V. PHASE DIAGRAM

The biggest challenge in determining the numerical phase diagram of this system is the highly nonconvex nature of the energy landscape in the regimes with strong DDI, where the simulations converge to different local minima for different initial guesses irrespective of the numerical methods used. For purely magnetic crystals this is taken care of by starting from different multi-Gaussian *Ansätze* and comparing their final energies [43]. However, when the applied light fields E_0 are also increased, not only are the energetically dense local minima potentially numerous but also the choice of initial guesses is no longer obvious. Therefore, convergence to the true global minimum remains ambiguous. In Fig. 2(a) we parametrize the nonconvexity of the energy landscape via the maximum energy difference ΔE obtained from different initial *Ansätze*. Deviation of ΔE from zero indicates that the converged solutions are quasistationary states, associated with different

local minima. The recovery of convexity in the energy landscape for high E_0 can be intuitively attributed to the curing of the unstable magnetic roton due to increasing LII.

Interestingly, the nonconvexity does not hinder the detection of the phase boundaries as the qualitative nature of the density patterns obtained from all initial guesses remains same (we provide the expressions for the different initial guesses used in Appendix B). To obtain the structural transition boundaries we focus on three key observables, namely, the reflection coefficient r_c (defined in Appendix A) which measures the backreflection of the incoming light fields due to the dynamic formation of a density grating, the density contrast $\Delta n = |n_{\text{max}} - n_{\text{min}}|/(n_{\text{max}} + n_{\text{min}})$ in the bulk of the condensate, and the superfluid fraction $f_s = (L/n)(\int |\psi|^{-2} dz)^{-1}$ [38,44,45]. The mean-field phase diagrams are shown in Fig. 2 in the parameter space of g_d/g and E_0 .

The reflection coefficient r_c acts as a robust parameter to detect the onset of dominant light effects and as a nondestructive experimental probe of the emergent light crystalline and light-magnetic crystalline order. Although the excitation spectrum boundaries are in qualitative agreement with the numerical simulations, the influence of the box-potential-induced edge effects lowers the threshold E_0 at which LII effects can become prominent, as seen in Fig. 2(b). It is further lowered at $g_d/g \gtrsim 1.35$ when strong DDI leads to increasingly denser droplets. This effect is captured by the increase in r_c as the medium gets more opaque from the LC phase to the LMC phase. Additionally, the structural transition curve from the MC phase to the LMC phase is much steeper than that from the S phase to the LC phase due to higher g_d/g . We find that this transition region precisely hosts the droplets of supersolid phase and demarcates the same in Fig. 2(b). Furthermore, the nonconvexity of the energy landscape can also be seen in the behavior of r_c (see Appendix A). The contrast Δn is used to faithfully mark any transition from the S to the crystalline phases (LC, MC, and LMC) and varies smoothly across the crystalline phases [see Fig. 2(c)].

Finally, the superfluid fraction f_s shown in Fig. 2(d) decreases as g_d/g increases for any fixed E_0 in the LC and LMC phases. For $g_d/g \gtrsim 1.5$, there is a recovery of superfluidity as the LMC phase is entered from the MC phase accompanied by the emergence of the peculiar droplets of supersolid states. Clearly, light-induced interactions play a significant role in enhancing the supersolid properties. This is further validated by evaluating the phase coherence [46] in numerical simulations of the state preparation including thermal noise (see Appendix C).

VI. STATE PREPARATION AND DYNAMICS

Finally, we demonstrate in Fig. 3 that despite the nonconvexity of the energy landscape, all crystalline phases can be prepared dynamically. This is in contrast to a recent work where the combination of nonconvexity and symmetry led to amorphous behavior for a self-organized BEC in a cavity with Rydberg-excitation-induced long-range interactions [47]. For the experimentally relevant $d = 10 \mu_B$ (Dy atoms) and $\omega_\rho/2\pi = 100$ Hz, beginning with a uniform bulk condensate at $a = 100a_0$ and $E_0 = 0$ in the S phase, the three different crystal phases are obtained by either quenching g_d/g

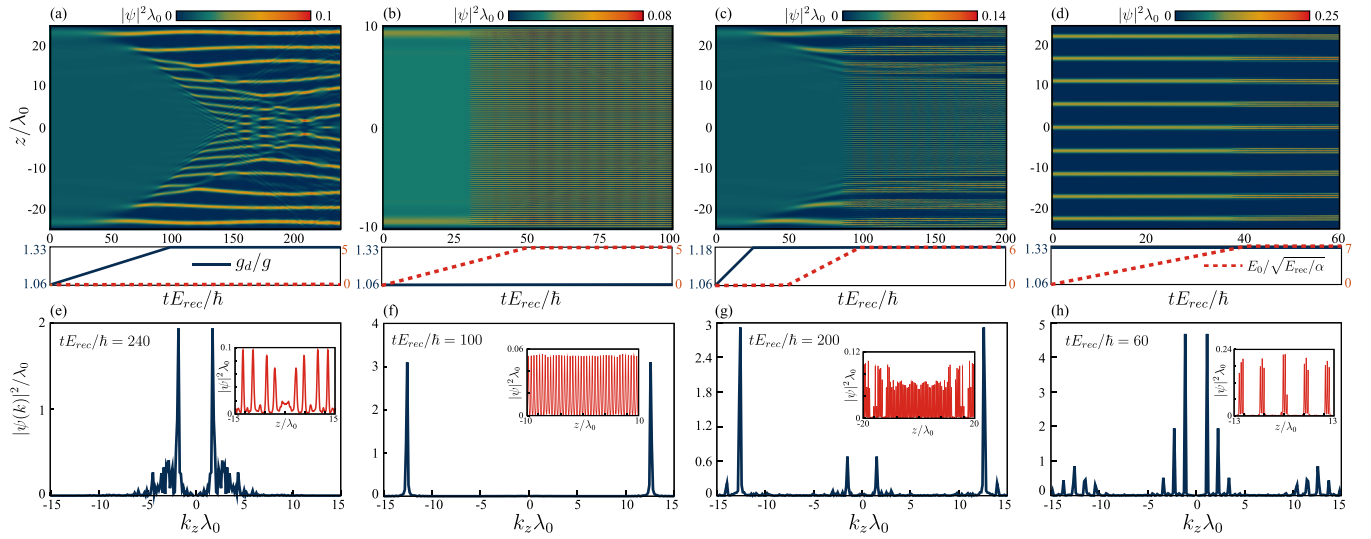


FIG. 3. Preparation of (a) MC, (b) LC, and (c) LMC states starting from an unordered state and (d) the LMC state starting from a MC for Dy atoms with their corresponding ramping schemes of g_d/g and the light intensities E_0 shown in the middle row. (e)–(h) Corresponding densities in momentum space at the final time. For concreteness, the final-time density distributions in real space are shown in the insets. All other parameters are the same as in Fig. 1(b).

(by varying a) or ramping E_0 up in a box trap. The sweeping schemes are plotted in the second row of Figs. 3(a)–3(c).

The dynamics reveals several crucial distinctions between the emergence of the MC [Fig. 3(a)] vs the LC [Fig. 3(b)]. In the MC, the crystalline order sets in locally from the edges [48] and grows towards the center, while in the LC, the onset of order is sharp and global. The MC excitation due to the sweeping involves both lattice vibrations and amplitude oscillations. In contrast, the phononic modes are almost frozen for the LC once it sets in. This pinning effect is a by-product of the singularly dominant momentum peak at $\pm 2k_{\text{eff}}$ as well as the light-field boundary conditions.

During the emergence of the LMC phase [see Fig. 3(c)] both these behaviors are observed as g_d/g and E_0 are swept sequentially. Interestingly, depending on the holding time after g_d/g is quenched and before E_0 is ramped, very different LMC density patterns can be obtained due to the pinning effect. In Fig. 3(d) the MC is chosen as the initial state, as opposed to the homogeneous state in Figs. 3(a)–3(c). This provides greater control over the desired LMC state. For example, the droplets of supersolid state can be prepared by ramping E_0 , which allows the deterministic manipulation of the intradroplet contrast. The momentum space distribution and spatial patterns (inset) of the densities at final times are illustrated in Figs. 3(e)–3(h). A visual comparison between Figs. 3(e) and 3(f) clearly shows that the fat-tailed distribution in the case of the MC correlates with the softness of the crystalline order, while the single peak corresponding to the LC indicates the stiffness of the spatially pinned LC [49]. In Appendix C we supplement the ideal state preparation dynamics presented here with those including thermal noise and find good qualitative agreement between them.

VII. CONCLUSION AND OUTLOOK

We have demonstrated that competing long-range interactions in a laser-driven dipolar BEC can lead to a rich phase diagram with a variety of crystalline phases. An important challenge to realize the predicted crystalline structures is to minimize the laser-induced heating rate which scales as $R \sim (\Gamma^3/8\Delta_a^2)(I/I_{\text{sat}})$ for an optical transition with linewidth Γ , detuning Δ_a , saturation intensity I_{sat} , and laser intensity $I = c\epsilon_0|E_0|^2/2$. We show in detail in Appendix E that this heating rate takes manageable values in state-of-the-art setups with erbium or dysprosium BECs. For instance, the 741-nm transition of Dy with $\Gamma = 2\pi \times 1.8$ KHz, a laser intensity $I = 0.6$ W/cm², and detuning $\Delta_a = 2\pi \times 1.6$ MHz leads to $R \sim 34$ Hz. Comparing this to our state preparation timescales of approximately $100\hbar/E_{\text{rec}}$, it becomes clear that the phases we predict are achievable in current experimental setups. Our work also opens up a promising direction for next-generation experiments and theoretical studies involving dipolar BECs where the addition of a laser drive would lead to fascinating phenomena. Some pertinent follow-up questions, to be addressed elsewhere [50], include a detailed analysis of the phase coherence in the LMC phase (beyond what is presented in Appendix C) and the impact of harmonic trapping in the axial z direction.

ACKNOWLEDGMENTS

C.M. acknowledges support from IIT Gandhinagar via the Early Career Fellowship program. S.O. was supported by a postdoctoral fellowship of the Max Planck Harvard Research Center for Quantum Optics. F.M. acknowledges financial support from the stand-alone Project No. P 35891-N

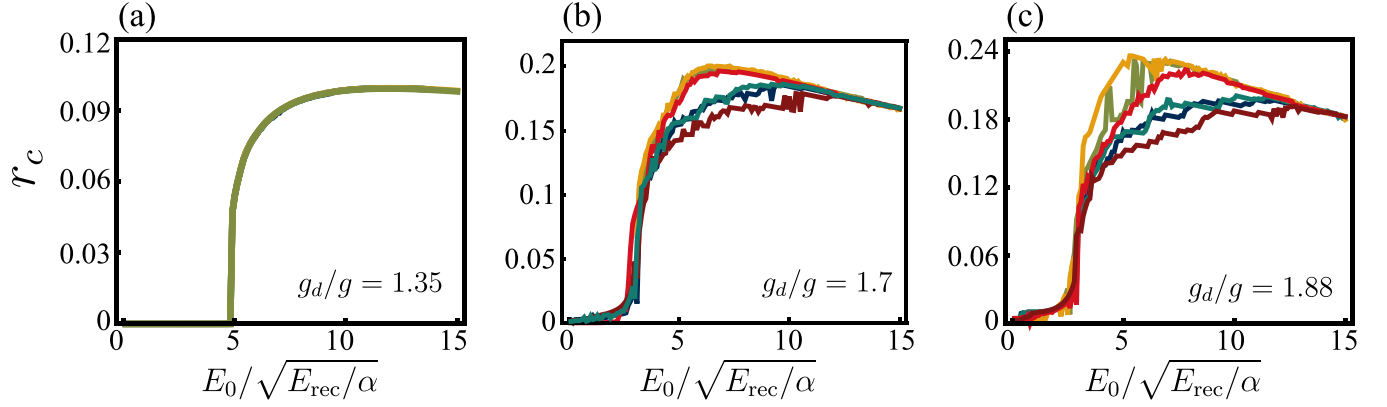


FIG. 4. Reflection coefficients r_c for converged states of eGPE obtained from different initial guesses for (a) $g_d/g = 1.35$, (b) $g_d/g = 1.7$, and (c) $g_d/g = 1.88$, corresponding to the same parameters used in Fig. 1(b).

of the Austrian Science Fund (FWF) and the FET Network Cryst3 funded by the European Union via Horizon 2020. F.M. and B.P.V. acknowledge support from an India-Austria DST-BMWF joint project, Projects No. IN 05/2020 and No. DST/INT/BMWF/AUSTRIA/P-06/2020, respectively.

APPENDIX A: HELMHOLTZ EQUATION SOLUTION

We now detail the procedure to solve the Helmholtz equation specified by Eq. (2) [or in Eq. (7) in a dimensionless form] for a given condensate order parameter $\psi(z, t)$ inside the finite-size box potential extending within $-L/2 < z < L/2$. Consider the incident beam on the BEC of size L from the left. The boundary conditions to solve the Helmholtz

equation for either the left or the right propagating light field within the BEC can be determined by first recognizing that the light field to the left of the condensate is given by $E^{\text{left}}(x) = Ae^{ik_0(x+L/2)} + Be^{-ik_0(x+L/2)}$ and the field to the right is given by $E^{\text{right}}(x) = De^{ik(x-L/2)}$ [10]. The relation between the incident (A), reflected (B), and transmitted (D) amplitudes is given by

$$B = r_c A, \quad (\text{A1})$$

$$D = t_c A \quad (\text{A2})$$

and defines the reflection and transmission coefficients r_c and t_c , respectively. Note that $|r_c|^2 + |t_c|^2 = 1$. The electric field at the boundary of the BEC is

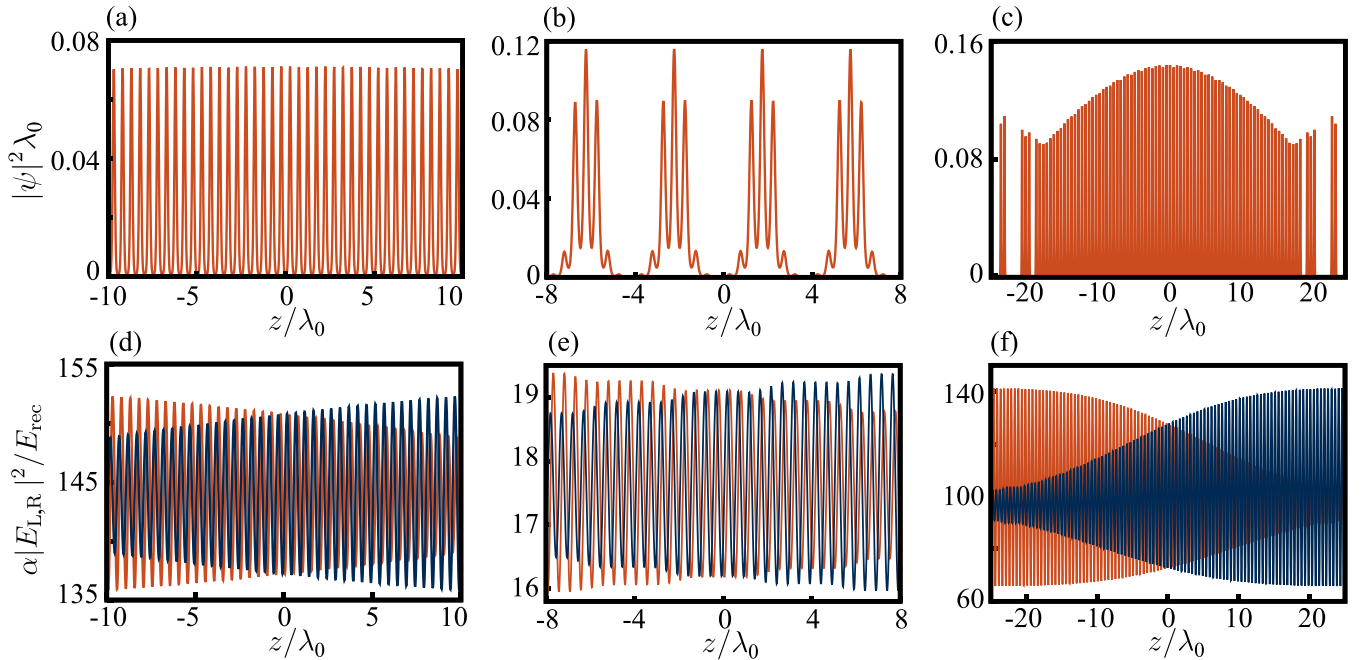


FIG. 5. (a) and (b) Density profiles shown in Figs. 1(d) and 1(e), respectively. (c) Density profile corresponding to $\{g_d/g, \sqrt{\alpha}E_0/E_{\text{rec}}\} = \{1.7, 10\}$ with all other parameters the same as in Figs. 1(d) and 1(e). (d)–(f) Light field intensity profiles corresponding to (a)–(c), respectively, obtained from the solution of the Helmholtz equation; the curves with the decreasing (increasing) amplitude of oscillations as a function of z represent $|E_L|^2$ ($|E_R|^2$).

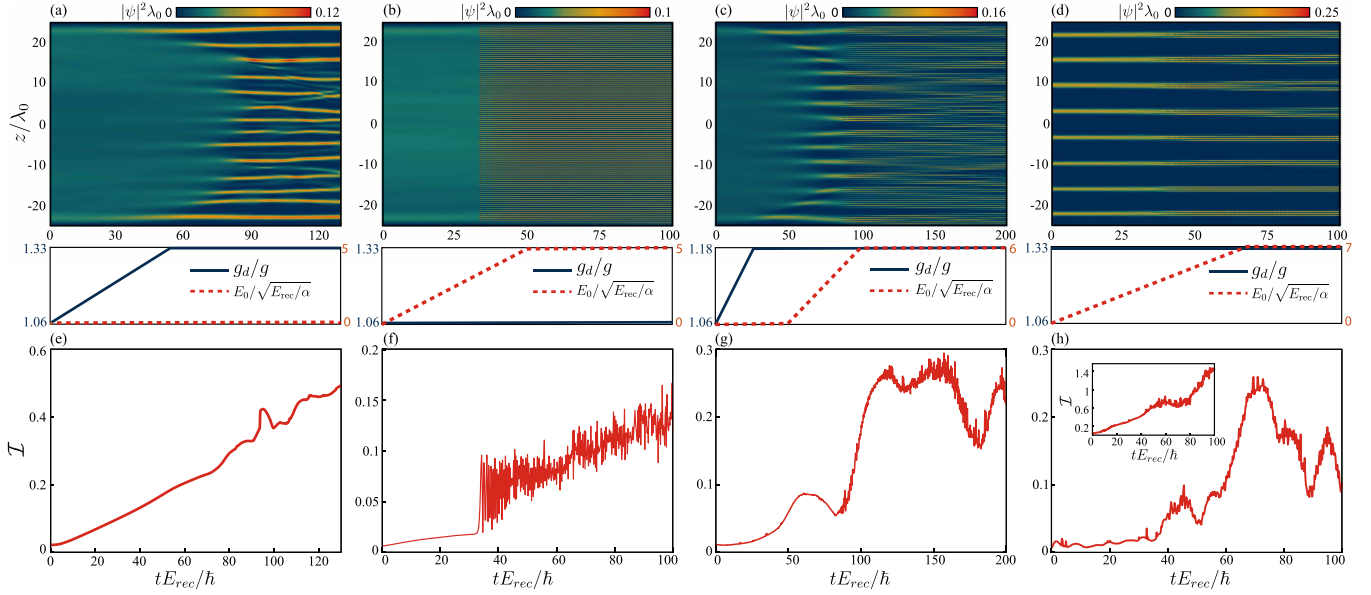


FIG. 6. Preparation of (a) MC, (b) LC, and (c) LMC states starting from an unordered state with additional thermal noise and (d) a LMC starting from a MC with added thermal noise for Dy atoms with their corresponding ramping schemes of g_d/g and the light intensities E_0 shown in the middle row, the same as in Fig. 3. (e)–(h) Corresponding incoherence plots with time, which is an average of at least three pairs of droplets where the droplets have length scales of either (e) MC or (f)–(h) LC. The inset in (h) is the incoherence plot when the chosen droplets are of the MC length scale.

given by

$$\begin{aligned} E^{\text{left}}\left(-\frac{L}{2}\right) &= A + B, & \frac{\partial E^{\text{left}}}{\partial z}\left(-\frac{L}{2}\right) &= ik_0(A - B), \\ E^{\text{right}}\left(\frac{L}{2}\right) &= D, & \frac{\partial E^{\text{right}}}{\partial z}\left(\frac{L}{2}\right) &= ik_0D. \end{aligned} \quad (\text{A3})$$

In order to compute r_c we take an arbitrary value for the incident amplitudes $E^{\text{left}}(-\frac{L}{2})$ and $\frac{\partial E^{\text{left}}}{\partial z}(-\frac{L}{2})$ as the Cauchy boundary condition and solve the Helmholtz equation in the region $-\frac{L}{2} \leq z \leq \frac{L}{2}$ using the fourth-order Runge-Kutta method. This allows us to determine $E^{\text{right}}(\frac{L}{2})$ and $\frac{\partial E^{\text{right}}}{\partial z}(\frac{L}{2})$. From the ratios $r_1 = E^{\text{left}}(-\frac{L}{2})/E^{\text{right}}(\frac{L}{2})$ and $r_2 = \dot{E}^{\text{left}}(-\frac{L}{2})/\dot{E}^{\text{right}}(\frac{L}{2})$ (where $\dot{E} = \frac{\partial E}{\partial z}$), we obtain the reflection coefficient as

$$r_c = \frac{r_1 - r_2}{r_1 + r_2} \quad (\text{A4})$$

for a given atomic order parameter $\psi(z, t)$. Once we have r_c , we can now set the amplitude of the incident light as the laser driving field amplitude $A = E_0$ and solve the Helmholtz equation with boundary conditions given by Eqs. (A1)–(A3) to determine $E_L(z)$. A similar approach can be used to solve for $E_R(z)$ using the light beam incident from the right. Since we have only considered symmetric driving strength from the left and right, we will get the same r_c for both cases. As we saw in Fig. 2, r_c is a good order parameter for identifying the different ordered crystalline phases. Moreover, as we show in Fig. 4, r_c also clearly tracks the nonconvexity of the energy landscape of converged eGPE solutions. We see clearly that r_c shows oscillations in the same region with $\Delta E \neq 0$ in Fig. 1(b), indicating the curing of the MRI due to the LII for higher E_0 values.

As an example of the behavior of the electric fields, in Fig. 5 we plot densities and their corresponding left and right propagating light fields corresponding to Figs. 1(d) and 1(e) and for a region with both strong LII and DDI [Fig. 5(c)]. The development of a periodic potential breaking the translation symmetry of the light field intensity accompanying the development of the periodic crystalline structures for the atomic density is clearly shown. One feature to note in Fig. 5 is that in general we find that the peak intensity of the standing-wave light monotonically decreases (in the direction of propagation of the applied traveling wave) in a region with an atomic density wave. Interestingly, this feature helps us also identify gaps between atomic density waves as in Figs. 5(b) and 5(e) by noticing that the peak intensity is preserved in atomic grating free regions.

APPENDIX B: INITIAL GUESSES

The different initial guesses used to obtain Fig. 2 are either multi-Gaussian (ψ_{Gaussian}), tanh (ψ_{tanh}), or Thomas-Fermi (ψ_{TF}) profiles, where

$$\begin{aligned} \psi_{\text{Gaussian}} &= \mathcal{A}_{\text{Gaussian}} \sum_{i=1}^{\nu} e^{-(z-z_i)^2/2\sigma^2}, \\ \psi_{\text{tanh}} &= \mathcal{A}_{\text{tanh}} \sqrt{\tanh(z+\sigma) - \tanh(z-\sigma)}, \\ \psi_{\text{TF}} &= \mathcal{A}_{\text{TF}} \sqrt{1 - \frac{z^2}{\sigma^2}}. \end{aligned}$$

The prefactors \mathcal{A}_j for $j \in [\text{Gaussian}, \text{tanh}, \text{TF}]$ are normalization constants and σ is proportional to the spatial widths. In the case of multi-Gaussian *Ansätze* we have used cases with $6 \leq \nu \leq 10$ and $\sigma/\lambda_0 \sim 2$. For tanh and Thomas-Fermi

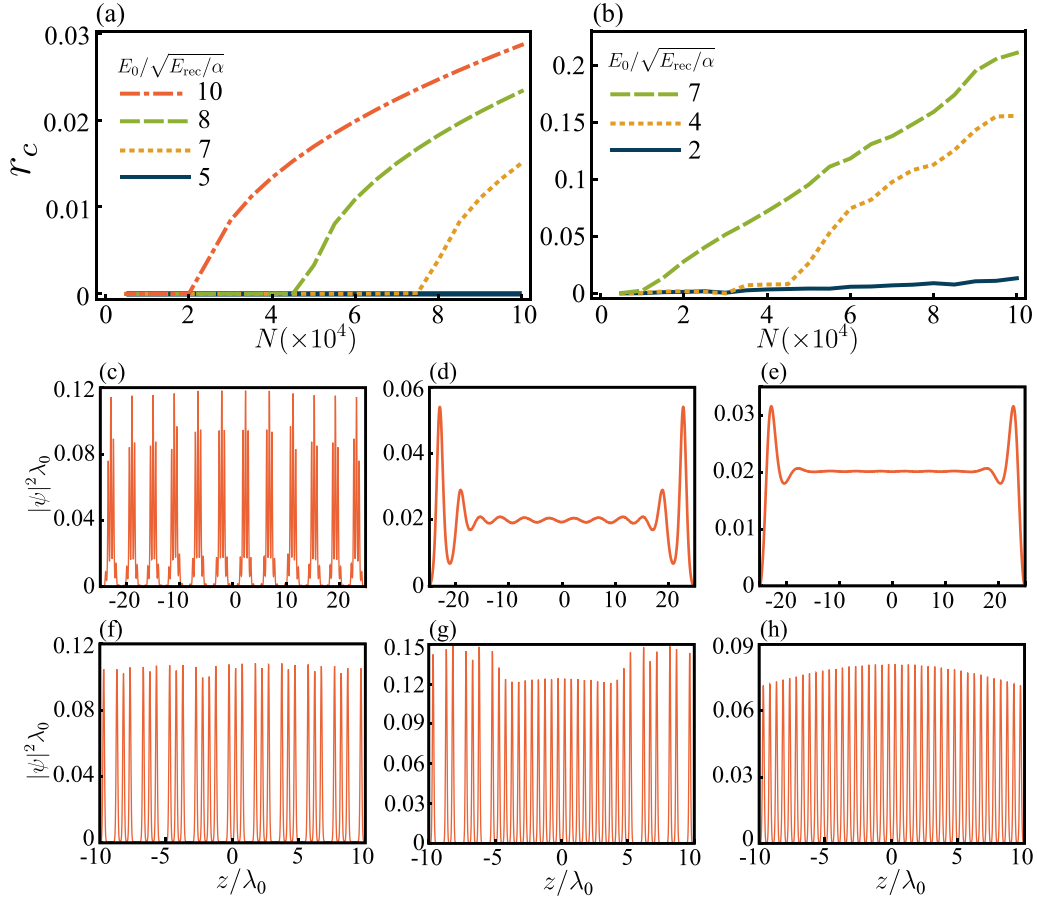


FIG. 7. Threshold value of the LC captured by the parameter r_c as N is varied for (a) $g_d/g = 0.9$ and (b) $g_d/g = 1.88$ with the other parameters similar to those in Fig. 1. (c)–(h) Two cases from the LMC phase where gradually reducing N results in shifts of the phase boundaries and the LMC state either changing to an MC and eventually unordered state or changing into an LC state. (c)–(e) correspond to Fig. 1(e) except with (d) $N = 80000$ and (e) $N = 50000$. (f)–(h) correspond to Fig. 1(f) with (g) $N = 50000$ and (h) $N = 10000$.

Ansätze σ has been chosen such that $|\psi_{\text{tanh, TF}}|^2$ spans the entire numerical box width.

In the LMC phase, the energy landscape consists of numerous local minima around the global minima for strong DDI. For S different *Ansätze* listed above, solutions converge to qualitatively similar yet quantitatively different ground states with P different energy values (E_p with $p \in P$) where $P \leq S$. We employ the parameter $\Delta E = |E_p^{\text{max}} - E_p^{\text{min}}|$, the span between the maximum and minimum energies obtained from S different initial guesses, to characterize the nonconvexity of the energy landscape. We used $S = 6$ for Fig. 2.

APPENDIX C: COHERENCE PROPERTIES

We aim to quantify the coherence properties, following Ref. [46], of different types of crystals generated in Fig. 3. In Figs. 6(e)–6(h) we plot the incoherence \mathcal{I} , where the value zero signifies coherence and $\pi/2$ refers to incoherence. At time $t = 0$ we have included noise in our initial state as

$$\psi(z) = \psi_0(z) + \sum_n \alpha_n \phi_n(z), \quad (\text{C1})$$

where $\phi_n(z)$ are single-particle states and α_n are complex Gaussian random variables that obey the relation

$$\langle |\alpha_n|^2 \rangle = (e^{\epsilon_n/k_B T} - 1)^{-1} + \frac{1}{2}. \quad (\text{C2})$$

We have restricted the sum to condition that $\epsilon_n \leq 2k_B T$ with $T = 10$ nK. The initial noise plays an important role in the emergence of instabilities while quenching sequences. Consequently, the dynamic phase incoherence is given by

$$\mathcal{I}(t) = \frac{\int_{\mathcal{C}} dz |\psi(z, t)|^2 [\theta(z, t) - \langle \theta(z, t) \rangle]}{\int_{\mathcal{C}} dz |\psi(z, t)|^2}. \quad (\text{C3})$$

The phase is denoted by $\theta(z, t)$ and $\langle \theta(z, t) \rangle$ is chosen such that \mathcal{I} is minimized at every iteration.

We evaluate incoherence between at least three pairs of droplets (of smallest length scale) and average over them for all cases. A comparison between Figs. 6(a) and 6(b) clearly shows that the coherence is better maintained in the LC phase, though as time progresses both monotonically lose coherence. In Figs. 6(c) and 6(d) the behavior of coherence is extremely nonmonotonic, but still the incoherence remains small in comparison to purely magnetic crystals. In fact, both these cases display significant recovery of coherence after the light amplitude quench and formation of light crystals.

APPENDIX D: DEPENDENCE ON THE NUMBER OF ATOMS

In this Appendix we aim to have a preliminary understanding of the behavior of the ordered phases of Fig. 2 with respect to a change in the number of atoms. In the case of MC phases this has been thoroughly covered both experimentally [31] and theoretically [33,43] in previous studies. We will focus on the LC and LMC phases.

The behavior of the LC phase with respect to the number of atoms is well captured by the r_c . In Fig. 7 the two extreme cases of $g_d/g = 0.9$ and 1.88 with respect to number of atoms are shown for different light amplitudes. As the number of atoms decreases, the LC is eventually lost. This behavior can be understood by the density dependence of the optical potential. A higher density enhances the coupling and in turn precipitates the LC phase. The loss of crystal order at lower N can then be compensated by increasing the light intensity. Note that the curves in Fig. 7(a) are smoother than those in Fig. 7(b) because in the latter case, nonconvexity of the energy functional makes it difficult to determine the true ground state quantitatively.

The characterization of LMC states with N is however non-trivial. We have used the same parameters used in Figs. 1(e) and 1(f) to highlight the contrasting behavior the density patterns can show when N is reduced. In Figs. 7(c)–7(e) we begin with $N = 10^5$ with a droplets of supersolid density pattern. When atom numbers are reduced there is a quick change in phase and the light crystalline order is lost to give rise to a density modulated state with the length scale of the MC. Further reduction in N results in an unordered state. On the other hand, in Figs. 7(f)–7(h) we begin with a state closer to the LC-LMC boundary. Here reduction of atoms eventually results in obtaining a LC phase. This would eventually be lost to give an unordered state in accordance with the behavior displayed in Fig. 7(a).

APPENDIX E: HEATING RATE CALCULATION

The frequency-dependent polarizability of a two-level atom subject to a light field with detuning Δ_a is given by [for $\Delta_a \gg \Gamma$, with Γ denoting the linewidth (spontaneous emission rate) of the transition] [51]

$$\alpha(\omega) = \frac{\alpha_0 \omega_0^2}{\omega_0^2 - \omega^2} \approx \frac{\omega_0 \alpha_0}{2\Delta_a}, \quad (\text{E1})$$

where $\alpha_0 = 2\mu^2/\hbar\omega_0$ is the static polarizability for a transition frequency ω_0 and transition electric dipole moment μ . Note that the light-atom coupling parameter $\zeta = \alpha N/2\pi\epsilon_0\lambda_0 l^2$ is determined by the polarizability $\alpha(\omega)$. Since in all calculations presented in the main text we chose $\zeta = 0.1$, we will choose detuning Δ_a to ensure this is satisfied. The heating rate due to spontaneous emission for atoms subject to light of intensity I is given by

$$R = \frac{\Gamma^3}{8\Delta_a^2} \frac{I}{I_{\text{sat}}}, \quad (\text{E2})$$

TABLE I. Detuning Δ_a and heating rates for different lines of Dy with $(N, A \equiv 2\pi l_\rho^2) = (10^5, 4 \times 10^{-12} \text{ m}^2)$.

$\lambda_0(\text{nm})$	$I(\text{W}/\text{m}^2)$	$\Gamma(\text{Hz})$	$\mu(\text{D})$	$\alpha(\text{Hz cm}^2/\text{V}^2)$	$\Delta_a(\text{MHz})$	$R(\text{Hz})$
1001	3×10^3	330	0.032	$265h$	0.5	20
741	4.4×10^3	1.12×10^4	0.12	$370h$	10	34
626	5×10^3	8.5×10^5	0.81	$337h$	500	52
598	5×10^3	7.7×10^4	0.22	$332h$	50	59
421	7.3×10^3	2×10^8	6.93	$221h$	5.5×10^4	113

with the saturation intensity I_{sat} given by

$$I_{\text{sat}} = \frac{2\pi\hbar\omega_0\Gamma}{6\lambda_0^2} \quad (\text{E3})$$

for a two-level atom model. Focusing on dysprosium, we find that the data for Γ and I_{sat} for different optical transitions are presented in Ref. [52]. Since the dipole moment strength μ is not directly available, we estimate the same using Eq. (E3) and the expression for spontaneous emission rate of a two-level atom $\Gamma = \omega_0^3 \mu^2 / 3\pi\epsilon_0 \hbar c^3$ as

$$\mu = \sqrt{\frac{c\epsilon_0 \hbar^2 \Gamma^2}{4I_{\text{sat}}}},$$

with c and ϵ_0 denoting the speed of light and permittivity of free space, respectively. Choosing the $\lambda_0 = 741$ nm transition in Dy with $I_{\text{sat}} = 0.57 \mu\text{W}/\text{cm}^2$ and $\Gamma = 1.12 \times 10^4$ Hz [52], we find that a detuning of $\Delta_a \sim 2\pi \times 1.6$ MHz leads to $\zeta = 0.1$ for our chosen system parameters with $N = 10^5$ atoms confined in a transverse trap $\omega_\rho/2\pi = 100$ Hz. Note that we use the transverse trap frequency to estimate the cross section as $l^2 \sim l_\rho^2 = \hbar/m\omega_\rho$ in the expression of ζ . This leads to the estimate of the heating rate of $R \sim 34$ Hz presented in the main text.

For the sake of completeness and to show that there is enough room in terms of choice of experimental parameters, we first present Table I, which gives the detuning Δ_a choices and heating rates for different lines of Dy with $(N, A \equiv 2\pi l_\rho^2) = (10^5, 4 \times 10^{-12} \text{ m}^2)$. In a similar manner we also find the possibilities for erbium with $(N, A) = (5 \times 10^5, 4 \times 10^{-12} \text{ m}^2)$ in all cases, listed in Table II.

TABLE II. Same as Table I but for Er with $N = 5 \times 10^5$.

$\lambda_0(\text{nm})$	$I(\text{W}/\text{m}^2)$	$\Gamma(\text{Hz})$	$\mu(\text{D})$	$\alpha(\text{Hz cm}^2/\text{V}^2)$	$\Delta_a(\text{MHz})$	$R(\text{Hz})$
1299	1.1×10^4	5.6	0.006	142	$0.07h$	6
841	1.7×10^4	5×10^4	0.3	93	$250h$	6
631	1.8×10^4	1.8×10^5	0.37	91	$400h$	13
582	1.8×10^4	1×10^6	0.77	90	$1700h$	18
400	1.7×10^4	1.7×10^8	5.85	91	95000	55

- [1] N. Defenu, T. Donner, T. Macri, G. Pagano, S. Ruffo, and A. Trombettoni, [arXiv:2109.01063](https://arxiv.org/abs/2109.01063).
- [2] L. Santos, G. V. Shlyapnikov, P. Zoller, and M. Lewenstein, *Phys. Rev. Lett.* **85**, 1791 (2000).
- [3] T. Lahaye, C. Menotti, L. Santos, M. Lewenstein, and T. Pfau, *Rep. Prog. Phys.* **72**, 126401 (2009).
- [4] M. A. Baranov, M. Dalmonte, G. Pupillo, and P. Zoller, *Chem. Rev.* **112**, 5012 (2012).
- [5] M. A. Norcia and F. Ferlaino, *Nat. Phys.* **17**, 1349 (2021).
- [6] L. Chomaz, I. Ferrier-Barbut, F. Ferlaino, B. Laburthe-Tolra, B. L. Lev, and T. Pfau, *Rep. Prog. Phys.* **86**, 026401 (2023).
- [7] S. Giovanazzi, D. O'Dell, and G. Kurizki, *Phys. Rev. Lett.* **88**, 130402 (2002).
- [8] D. H. J. O'Dell, S. Giovanazzi, and G. Kurizki, *Phys. Rev. Lett.* **90**, 110402 (2003).
- [9] J. Honer, H. Weimer, T. Pfau, and H. P. Büchler, *Phys. Rev. Lett.* **105**, 160404 (2010).
- [10] S. Ostermann, F. Piazza, and H. Ritsch, *Phys. Rev. X* **6**, 021026 (2016).
- [11] S. Ostermann, F. Piazza, and H. Ritsch, *New J. Phys.* **19**, 125002 (2017).
- [12] I. Dimitrova, W. Lunden, J. Amato-Grill, N. Jepsen, Y. Yu, M. Messer, T. Rigaldo, G. Puentes, D. Weld, and W. Ketterle, *Phys. Rev. A* **96**, 051603(R) (2017).
- [13] Y.-C. Zhang, V. Walther, and T. Pohl, *Phys. Rev. Lett.* **121**, 073604 (2018).
- [14] Y.-C. Zhang, V. Walther, and T. Pohl, *Phys. Rev. A* **103**, 023308 (2021).
- [15] B. Chatterjee and A. U. J. Lode, *Phys. Rev. A* **98**, 053624 (2018).
- [16] B. Chatterjee, C. Lévêque, J. Schmiedmayer, and A. U. J. Lode, *Phys. Rev. Lett.* **125**, 093602 (2020).
- [17] R. Mottl, F. Brennecke, K. Baumann, R. Landig, T. Donner, and T. Esslinger, *Science* **336**, 1570 (2012).
- [18] H. Ritsch, P. Domokos, F. Brennecke, and T. Esslinger, *Rev. Mod. Phys.* **85**, 553 (2013).
- [19] F. Mivehvar, F. Piazza, T. Donner, and H. Ritsch, *Adv. Phys.* **70**, 1 (2021).
- [20] P. Karpov and F. Piazza, *Phys. Rev. Lett.* **128**, 103201 (2022).
- [21] S. Gopalakrishnan, B. L. Lev, and P. M. Goldbart, *Nat. Phys.* **5**, 845 (2009).
- [22] A. J. Kollár, A. T. Papageorge, V. D. Vaidya, Y. Guo, J. Keeling, and B. L. Lev, *Nat. Commun.* **8**, 14386 (2017).
- [23] V. D. Vaidya, Y. Guo, R. M. Kroeze, K. E. Ballantine, A. J. Kollár, J. Keeling, and B. L. Lev, *Phys. Rev. X* **8**, 011002 (2018).
- [24] Y. Deng, J. Cheng, H. Jing, C.-P. Sun, and S. Yi, *Phys. Rev. Lett.* **108**, 125301 (2012).
- [25] S. Gopalakrishnan, I. Martin, and E. A. Demler, *Phys. Rev. Lett.* **111**, 185304 (2013).
- [26] X. Li, Q. Wang, H. Wang, C. Shi, M. Jardine, and L. Wen, *J. Phys. B* **52**, 155302 (2019).
- [27] F. Mivehvar, H. Ritsch, and F. Piazza, *Phys. Rev. Lett.* **123**, 210604 (2019).
- [28] L. Chomaz, D. Petter, P. Ilzhöfer, G. Natale, A. Trautmann, C. Politi, G. Durastante, R. M. W. van Bijnen, A. Patscheider, M. Sohmen, M. J. Mark, and F. Ferlaino, *Phys. Rev. X* **9**, 021012 (2019).
- [29] F. Böttcher, J.-N. Schmidt, M. Wenzel, J. Hertkorn, M. Guo, T. Langen, and T. Pfau, *Phys. Rev. X* **9**, 011051 (2019).
- [30] M. Guo, F. Böttcher, J. Hertkorn, J.-N. Schmidt, M. Wenzel, H. P. Büchler, T. Langen, and T. Pfau, *Nature (London)* **574**, 386 (2019).
- [31] L. Tanzi, E. Lucioni, F. Famà, J. Catani, A. Fioretti, C. Gabbanini, R. N. Bisset, L. Santos, and G. Modugno, *Phys. Rev. Lett.* **122**, 130405 (2019).
- [32] F. Wächtler and L. Santos, *Phys. Rev. A* **94**, 043618 (2016).
- [33] R. N. Bisset, R. M. Wilson, D. Baillie, and P. B. Blakie, *Phys. Rev. A* **94**, 033619 (2016).
- [34] L. Chomaz, R. M. W. van Bijnen, D. Petter, G. Faraoni, S. Baier, J. H. Becher, M. J. Mark, F. Wächtler, L. Santos, and F. Ferlaino, *Nat. Phys.* **14**, 442 (2018).
- [35] G. Natale, R. M. W. van Bijnen, A. Patscheider, D. Petter, M. J. Mark, L. Chomaz, and F. Ferlaino, *Phys. Rev. Lett.* **123**, 050402 (2019).
- [36] L. Landau, *Phys. Rev.* **60**, 356 (1941).
- [37] P. B. Blakie, D. Baillie, and S. Pal, *Commun. Theor. Phys.* **72**, 085501 (2020).
- [38] P. B. Blakie, D. Baillie, L. Chomaz, and F. Ferlaino, *Phys. Rev. Res.* **2**, 043318 (2020).
- [39] R. Ghosh, C. Mishra, L. Santos, and R. Nath, *Phys. Rev. A* **106**, 063318 (2022).
- [40] X. Antoine, A. Levitt, and Q. Tang, *J. Comput. Phys.* **343**, 92 (2017).
- [41] S. Ronen, D. C. E. Bortolotti, and J. L. Bohn, *Phys. Rev. A* **74**, 013623 (2006).
- [42] A. Janner, T. Janssen, and P. M. De Wolff, *Europhys. News* **13**, 1 (1982).
- [43] D. Baillie and P. B. Blakie, *Phys. Rev. Lett.* **121**, 195301 (2018).
- [44] A. J. Leggett, *Phys. Rev. Lett.* **25**, 1543 (1970).
- [45] N. Sepúlveda, C. Jossierand, and S. Rica, *Phys. Rev. B* **77**, 054513 (2008).
- [46] T. Bland, E. Poli, C. Politi, L. Klaus, M. A. Norcia, F. Ferlaino, L. Santos, and R. N. Bisset, *Phys. Rev. Lett.* **128**, 195302 (2022).
- [47] S. Ostermann, V. Walther, and S. F. Yelin, *Phys. Rev. Res.* **4**, 023074 (2022).
- [48] S. M. Rocuzzo, S. Stringari, and A. Recati, *Phys. Rev. Res.* **4**, 013086 (2022).
- [49] Y. Guo, R. M. Kroeze, B. P. Marsh, S. Gopalakrishnan, J. Keeling, and B. L. Lev, *Nature (London)* **599**, 211 (2021).
- [50] C. Mishra, S. Ostermann, F. Mivehvar, and B. P. Venkatesh (unpublished).
- [51] D. A. Steck, *Quantum and Atom Optics*, available at <http://steck.us/teaching> (2018), revision 0.12.2.
- [52] M. Lu, S. H. Youn, and B. L. Lev, *Phys. Rev. A* **83**, 012510 (2011).